Strongly suppressed proximity effect and ferromagnetism in topological insulator/ferromagnet/superconductor thin film trilayers of Bi_2Se_3/$SrRuO_3$/underdoped $YBa_2Cu_3O_x$: a possible new platform for Majorana nano-electronics

Gad Koren

Physics Department, Technion—Israel Institute of Technology Haifa, 32000, Israel

E-mail: gkoren@physics.technion.ac.il

CrossMark

Abstract

We report properties of a topological insulator–ferromagnet–superconductor trilayers comprised of thin films of 20 nm thick Bi_2Se_3 on 10 nm $SrRuO_3$ on 30 nm $YBa_2Cu_3O_x$. As deposited trilayers are underdoped and have a superconductive transition with T_c onset at 75 K, zero resistance at 65 K, T_{Cueri} at 150 K and T^* of about 200 K. Further reannealing under vacuum yields the 60 K phase of $YBa_2Cu_3O_x$ which still has zero resistance below about 40 K. Only when 10×100 microbridges were patterned in the trilayer, some of the bridges showed resistive behavior all the way down to low temperatures. Magnetoresistance versus temperature of the superconductive ones showed the typical peak due to flux flow against pinning below T_c, while the resistive ones showed only the broad leading edge of such a peak. All this indicates clearly weak-link superconductivity in the resistive bridges between superconductive $YBa_2Cu_3O_x$ grains via the topological and ferromagnetic cap layers. Comparing our results to those of a reference trilayer (RTL) with the topological Bi_2Se_3 layer substituted by a non-superconducting highly overdoped $La_{1.65}Sr_{0.35}CuO_4$, indicates that the superconductive proximity effect as well as ferromagnetism in the topological trilayer are actually strongly suppressed compared to the non-topological RTL. This strong suppression could originate in lattice and Fermi levels mismatch as well as in short coherence length and unfavorable effects of strong spin–orbit coupling in Bi_2Se_3 on the d-wave pairing of $YBa_2Cu_3O_x$. Proximity induced edge currents in the SRO/YBCO layer could lead to Majorana bound states, a possible signature of which is observed in the present study as zero bias conductance peaks.

Keywords: superconducting thin film multi-layers, critical currents, magnetic properties of thin films and interfaces, electron states at surfaces and interfaces, topological insulator, Majorana nano-electronics

(Some figures may appear in colour only in the online journal)

1. Introduction

Thin film junctions, bilayers and trilayers of a topological insulator (TI), a ferromagnet (FM) and a superconductor (SC), can exhibit many interesting phenomena such as triplet superconductivity [1–4], topological superconductivity [2, 5, 6], various proximity effects [7–11] and lead to the creation of exotic states including Majorana fermions (MF) [12–14]. All these phenomena involve strongly correlated electrons and the challenge is to understand the mutual effects of the interactions between the different comprising layers. We stress that the main signature of MFs in the experiments so far has been the observation of zero energy states which appeared as zero bias conductance peaks (ZBCPs) in conductance spectra. In order for these to be due to MFs however, it is necessary to show that they originate in the non-trivial topological phase of the system involved, and this was not yet demonstrated [12–14]. Moreover, ZBCPs can originate by other mechanisms such as Andreev reflections in unconventional SCs leading to zero energy bound states which are in the trivial regime [3, 4, 15–17]. Recent reports suggest ways to distinguish between observations of topological non-trivial and Andreev (trivial) ZBCPs [18, 19]. Thus, observation of ZBCPs alone can be consistent with the presence of MFs but not a definitive proof for their actual existence. Following our previous investigation on TI/FM bilayers of $Bi_{0.5}Sb_{1.5}Te_3/SrRuO_3$ (BST/SRO) where a robust magnetic proximity effect with the seemingly weak itinerant FM was found [11], we decided to extend our study to TI/FM/SC trilayers with the goal of creating spatially separated pairs of Majorana bound states (MBSs) in topological superconductors (TSCs). In the presence of the FM layer and the interface, time reversal and inversion symmetries are broken, thus in principle MBS in TSC in 2D can be formed in these trilayers [20, 21]. In the present paper we make an attempt to realize a 2D network of in-plane SC-TI/FM-SC junctions in TI/FM/SC thin film trilayers. An effort to fabricate networks comprised of 1D SC/TI nano-wires hosting MBSs was also recently reported [22]. These networks should allow for scaling up of the number of such devices (the MBSs at the ends of the wires) on a wafer, braiding them, and may open the way for Majorana nano-electronics for quantum computing.

When measuring transport properties with a bias current parallel to the interface of multi-layers which contain a superconducting layer, the problem is always shorting by the SC layer. This results from the zero resistance of the SC layer below T_c which carries all the current without observable influence of the other layers. To avoid this shorting effect, very thin SC layers should be used, or even better, layers of SC islands. In the cuprate this can be achieved by underdoping which depletes oxygen mostly from the inter-grain regions and rendering them non-superconducting. This was done in the present study, where TI/FM/SC trilayers of the topological insulator Bi_2Se_3 (BS), the itinerant ferromagnet $SrRuO_3$ (SRO) and the d-wave SC $YBa_2Cu_3O_x$ (YBCO) were used, with a ferromagnetic and superconducting transition temperatures of $T_{Curie} = 150$ K and $T_c = 60$ K, respectively.

Weak-link islands (or grains) superconductivity was found, where the coupling between the SC islands is via the TI/FM cap layers, forming a network of 1D current carrying channels. By comparing the results to those of a reference trilayer (RTL) where the TI layer is replaced by highly overdoped $La_{1.65}Sr_{0.35}CuO_4$ (LSCO35), we find that the superconductive proximity effect and ferromagnetism in the topological trilayer (TTL) are in fact strongly suppressed as compared to those of the non-topological RTL. By assuming proximity induced edge currents in the FM/SC bilayer by the TI at the interface, MBSs can be formed in the weak-link 1D channels.

2. Preparation and basic properties of the films and trilayers

Thin films of YBCO and SRO were chosen as the SC and FM for the present study since both are compatible and lattice matched with one another and grow epitaxially on (100) $SrTiO_3$ (STO), without inter diffusion between the layers. They are also very well characterized in the literature [23–25]. Bi_2Se_3 (BS) is the most well known TI and its thin films are also well characterized [26, 27]. These were used to prepare and investigate the TTLs of BS/SRO/YBCO. For comparison, a RTL was prepared without a topological layer. LSCO35 was chosen to substitute for the BS layer in the trilayer (yielding LSCO35/SRO/YBCO) since it is compatible with the base SRO/YBCO bilayer, grows epitaxially on it under the same deposition conditions, is non-superconducting and has a similar carrier concentration to that of the BS layer. All films were prepared on (100) STO wafers of 10×10 mm^2 area by pulsed laser deposition using the third-harmonic of a Nd-YAG laser. The laser was operated at a pulse rate of 3.33 Hz, with fluence of ~ 1.5 J cm^{-2} on the targets for the deposition of the epitaxial YBCO, SRO and reference LSCO35 films. Lower fluence of ~ 0.6 J cm^{-2} was used for the deposition of the BS layer. The SRO/YBCO bilayer as well as the LSCO35/SRO/YBCO trilayer were prepared *in situ* at 800 °C in one deposition run, while the BS film was deposited on the SRO/YBCO bilayer at 250 °C in a different vacuum chamber. The YBCO, SRO and LSCO35 films were deposited using stoichiometric ceramic targets of $YBa_2Cu_3O_x$, $SrRuO_3$ and $La_{1.65}Sr_{0.35}CuO_4$ under 70–90 mTorr of O_2 gas flow at 965 °C heater block temperature (about 800 °C on the surface of the wafer). The Bi_2Se_3 layers were deposited under vacuum using a pressed target with Bi to Se ratio of 1:17 at 300 °C heater block temperature (about 250 °C on the surface of the wafer). Electron dispersive spectroscopy measurements showed that disregarding the stoichiometry of the target, the resulting films had a Bi to Se ratio of 2:3 which is the stable Bi–Se phase. X-ray diffraction measurements showed that this film had the hexagonal Bi_2Se_3 structure, with preferential c-axis orientation normal to the wafer and $c = 2.84$ nm.

First annealing of the SRO/YBCO bilayer and LSCO35/SRO/YBCO trilayer was done *in situ* under 0.5 atm. of O_2
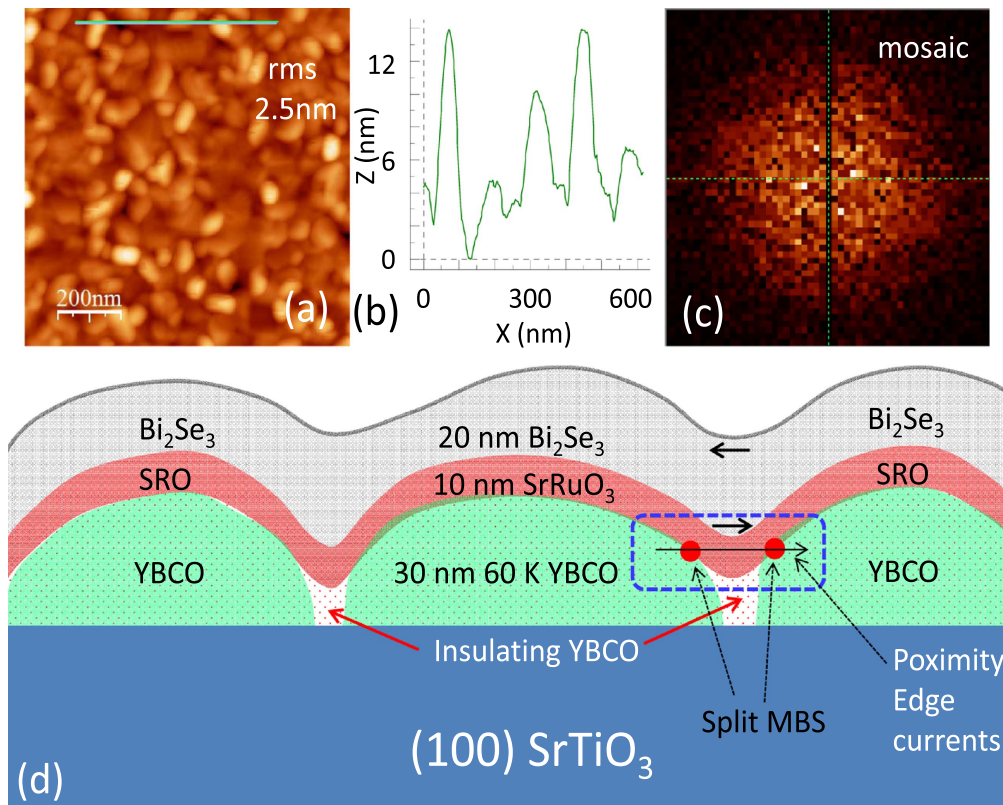
Figure 1. (a) Atomic force microscope image of the 20 nm BS on 10 nm SRO on 30 nm YBCO trilayer. Height profile along the line in (a) is shown in (b). Fourier transform of (a) is given in (c). (d) Depicts a schematic trilayer cross section model with three weakly linked YBCO islands. The enclosed area in the dashed rectangle shows a proposed scenario for the creation of split MBS similar to that described by Beenakker [20].

pressure with a dwell time of 1 h at 400 °C. This yielded well oxygenated samples with T_c of 88 K. Deposition of the BS layer on the SRO/YBCO bilayer (performed under vacuum at 250 °C) took about 20 min, after which the sample was rapidly cooled down to room temperature. This yielded the 'as deposited' TTL which was underdoped with T_c of 75 K, T_{Curie} of 150 K (SRO is insensitive to this vacuum annealing) and T^* of the pseudogap of underdoped YBCO at about 200 K. Further depletion of oxygen to obtain the 60 K YBCO phase, was done by annealing under vacuum at 250 °C for two more hours. This second annealing step was applied also to the RTL of LSCO35/SRO/YBCO. Patterning of the tri-layers was obtained by Ar-ion milling at 13 mA cm^{-2} and −180 °C, to minimize damage to the samples by heating during the milling process. Generally, ten equidistant micro-bridges of $10 \times 100 \, \mu m^2$ were patterned across the line dividing the wafer into two halves, with 1 mm distance between them. Forty $1 \times 1 \, mm^2$ contact pads were patterned on the two sides of the dividing line, 20 on each side. Transport measurements were carried out by the use of an array of 40 gold coated spring loaded spherical tips for the 4-probe dc measurements on ten different locations on the wafer, either with or without silver paste or gold contact pads. Magnetic fields of up to 8 T were applied normal to the wafer along the c-axis direction of the YBCO, BS and LSCO35 layers.

3. Results and discussion

We begin with characterizing the surface morphology, crystallization and in-plane order of the crystallites in the presently used TTL (20 nm BS/10 nm SRO/30 nm YBCO). Figure 1(a) shows an atomic force microscope image of a $1 \times 1 \, \mu m^2$ area of this TTL, while in (b) a typical height profile is shown along the line in (a). One can see good crystallization with rms roughness of 2.5 nm, which compared to the overall thickness of the TTL (60 nm), yields 4% roughness. Thus the TTL is quite smooth. The Fourier transform of (a) is given in (c) which reveals quite uniform angular intensity distribution in k-space, indicating mosaic in-plane order of the crystallites in real space. This is a result of a few different hexagonal in-plane orientations (see the bright spots in (c)) but without long range order. The fact that the BS layer is hexagonal here was established by the x-ray diffraction data where the hexagonal c-axis value was found (2.84 nm). Figure 1(d) depicts a schematic model for the underdoped TTL where three 60 K YBCO islands (or grains) are separated by narrow insulating YBCO regions (the white areas with red dots). These islands are nevertheless weakly connected via the BS/SRO cap layer, which leads to weak-link superconductivity between the grains via the proximity effect. Our results will be discussed in view of this model, and as we shall see they can be described well by it.
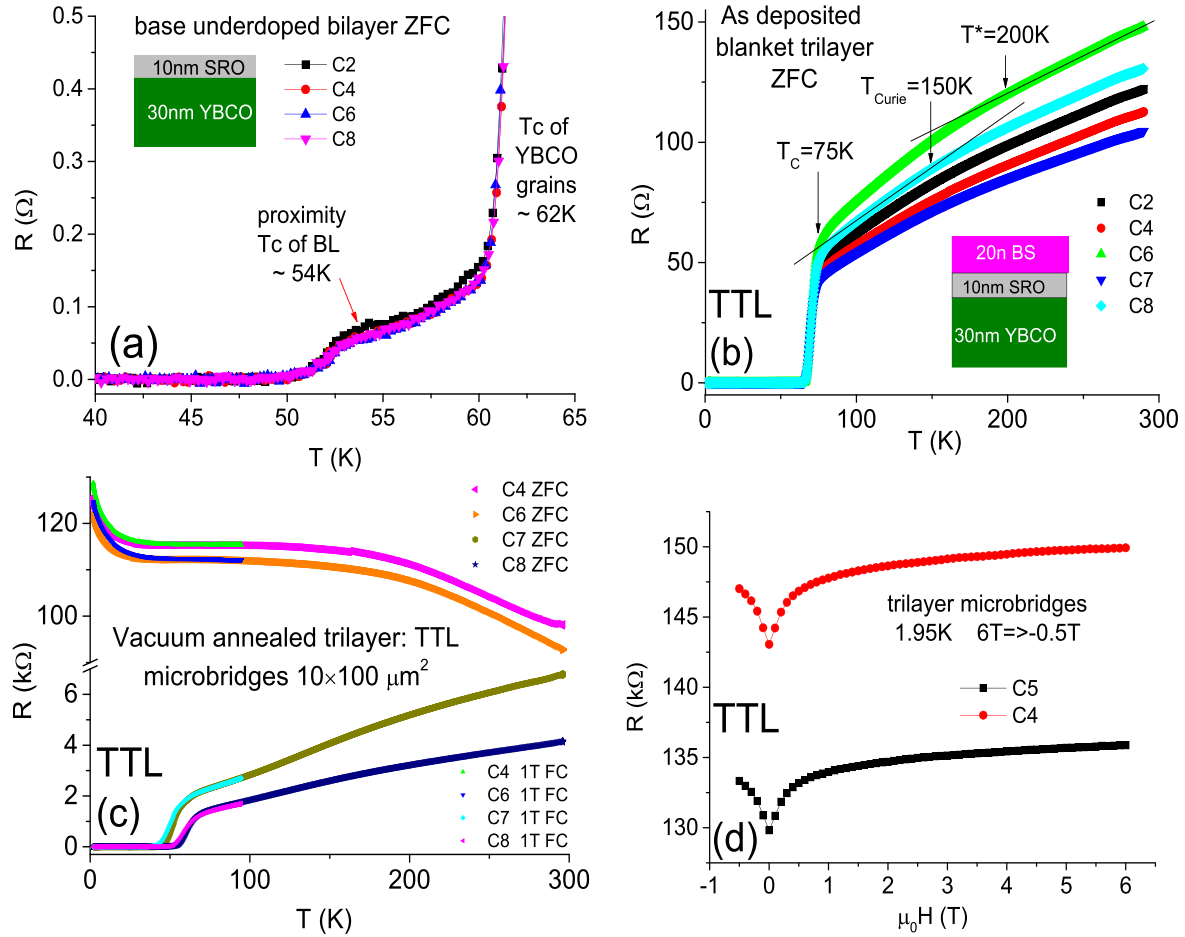
Figure 2. Resistance versus temperature of a blanket base bilayer of 10 nm SRO on 30 nm YBCO common to all trilayers in this paper is shown in (a). (b) Shows R versus T of the as deposited TTL of 20 nm thick BS on 10 nm SRO on 30 nm YBCO before patterning, while (c) shows it after patterning into ten $10 \times 100\ \mu m^2$ microbridges and further vacuum annealing. (a)–(c) Were measured under ZFC, and (c) also includes 1 T FC. (d) Depicts R versus magnetic field H of two resistive TTL microbridges of (c) at 1.95 K.

Figure 2(a) depicts R versus T results under zero field cooling (ZFC) measured at four different locations on a base bilayer of 10 nm SRO/30 nm YBCO which is common to all trilayers in the present paper. The main superconducting transition temperature of the underdoped YBCO layer is about 62 K. Below it, a second small proximity effect (PE) transition with $T_c \sim 54$ K can be seen (the knee in this curve). If the YBCO grains in this bilayer would have formed a continuous superconducting layer, then the bias current would flow through it masking any PE with the cap SRO layer. Thus the YBCO grains are separated by narrow insulating regions as depicted in figure 1(d), and the PE via the SRO cap layer is established. Figure 2(b) shows the as deposited R versus T results of the 20 nm BS/10 nm SRO/30 nm YBCO TTL which is underdoped with T_c of 75 K. The reason for the underdoping is that the topological BS layer is deposited at 250 °C under vacuum, and already at this temperature the YBCO layer loses oxygen, more so in the grain boundary regions (see figure 1(d) again). Nevertheless, the YBCO grains here are still connected too strongly, shorting the TTL below $T_c(R = 0) = 62$ K, with a small PE 'knees' above it up

to 65 K. Only after further two hours vacuum annealing at 250 °C, this TTL had $T_c(R = 0)$ of 50–53 K. Figure 2(c) shows R versus T results of four underdoped $10 \times 100\ \mu m^2$ microbridges patterned on this TTL. One set of data depicts ZFC results from room temperature down to 2 K, while the other represents 1 T field cooling (FC) data from 95 K down to 2 K. A striking result is that while the unpatterned sample shows transition to superconductivity all over the wafer with onset at 68 K, the microbridges show completely different results. Two of the bridges show a transition to superconductivity at 67 and 62 K with about 1 $\mu\Omega$ resistance below 53 and 45 K, respectively, whereas the other two are much more resistive at low temperatures and show insulating behavior versus T (note the broken ordinate scale in figure 2(c)). Clearly, the different locations of the bridges on the wafer sample different small areas of the trilayer, which either exhibit percolative superconductivity (as in C7 and C8) or not (as in C4 and C6). Figure 2(d) depicts R versus magnetic field H of two resistive TTL microbridges of (c) at 1.95 K. The result is very similar to the magnetoresistance of a stand-alone BS topological layer. It shows weak
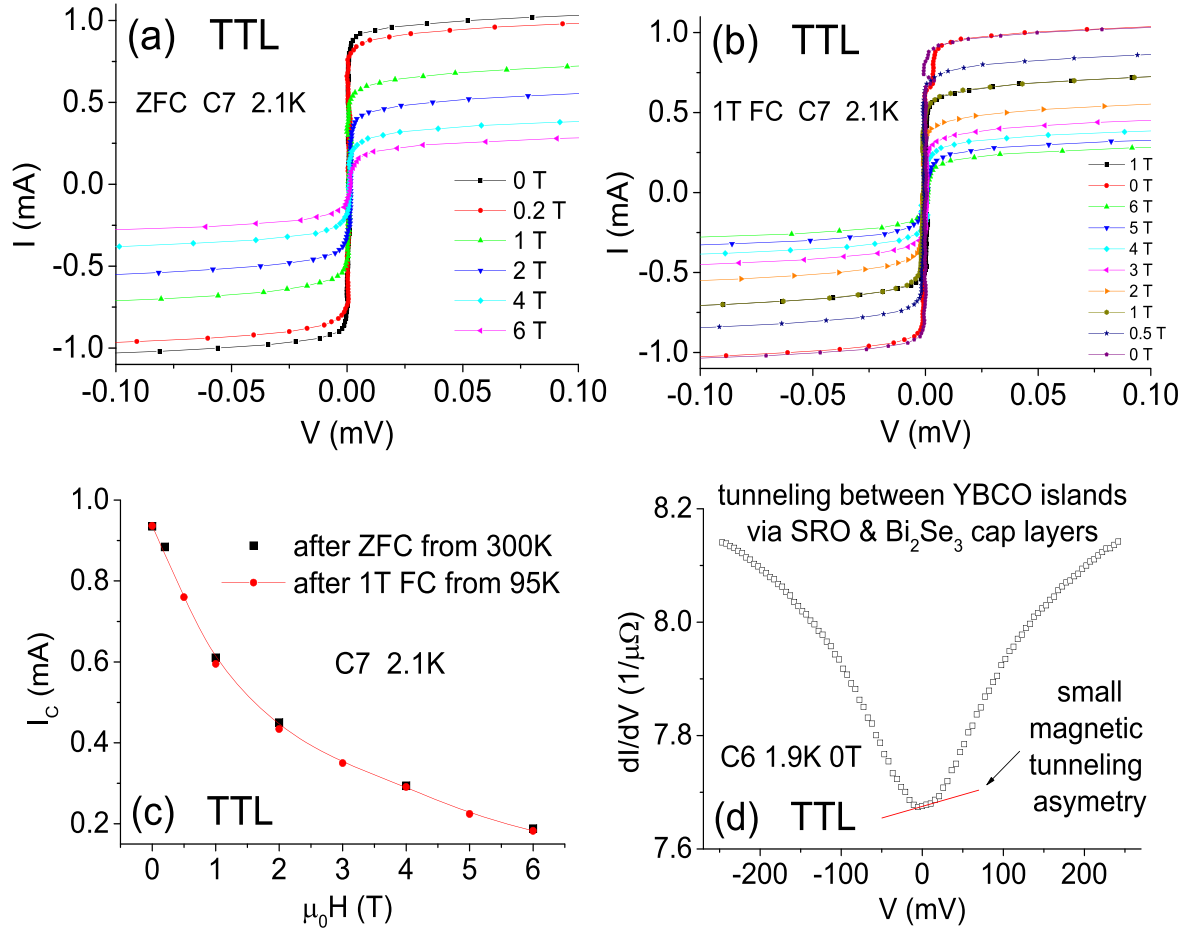
Figure 3. *I–V* curves of the C7 microbridge of the TTL of figure 2(c) at 2.1 K under different magnetic fields after two cooling conditions: ZFC from room temperature in (a) and 1 T FC from 95 K in (b). (c) Shows the critical currents I_c at 2.1 K versus field as deduced from the data of (a) and (b) using a 10 μV criterion. In (d) we plot a conductance spectrum of a resistive bridge (C6 of figure 2(c)) at 1.9 K and 0 T which shows a small asymmetry at low bias typical of magnetic tunneling junctions.

anti-localization (WAL) at low fields up to about 1 T with tendency to saturation above it [28, 29]. Unlike previous magnetoresistance results in bilayers of 15 nm BST/15 nm SRO where the WAL signature of the TI was observed together with that of the coercive field of the FM layer [11], here no effect of either the FM or SC layers is observed. This could be due to the fact that only a thinner FM layer of 10 nm SRO is used in the present study, but as we shall see later this is not the case, and both the superconductive PE and ferromagnetism are strongly suppressed in the present TTL.

Next we looked into the properties of the superconductive bridges of figure 2(c). Figure 3 depicts *I–V* curves (IVCs) at 2.1 K of the C7 bridge under various fields after ZFC (a), and after 1 T FC (b). The data looks very similar in both cases, as is even better seen in (c) where the critical current I_c deduced from this data using a 10 μV criterion is plotted versus field. Since vortex physics and pinning should depend on the cooling conditions under different magnetic fields and under field cycling, one would expect hysteresis effects in the IVCs and different I_c values under ZFC and 1 T FC. This however is not the case, apparently due to strong pinning in the YBCO islands and hardly any vortex motion at 2.1 K, except for the data of figure 3(b) at 0 T after 1 T FC and at 0 T after field cycling to 6

T and back to 0 T, where a vortex jump is observed at low positive bias. We have also found no hysteresis under field while measuring several IVCs of the C7 bridge at 2.1 K under increasing field up to 6 T and decreasing field back to 0 T (not shown). As no hysteresis effects were observed within the noise of the measurements, not under ZFC or FC conditions, neither under various fields and field cycling, we conclude that the magnetic properties of the trilayer are suppressed by the topological BS layer at the interface. Nevertheless, a weak signature of ferromagnetism is found in the resistive C6 bridge of figure 2(c), whose conductance spectrum at 1.9 K and under 0 T is shown figure 4(d). In this tunneling spectrum between SC islands, one can see a small asymmetry near zero bias which is typical of magnetic tunneling junctions [30, 31]. Thus the contribution of the ferromagnetic SRO layer to this spectrum is established.

To further explore the phenomena observed in the TTL of figure 2(c) where resistive and superconductive bridges were found on the same wafer, we measured the magnetoresistance MR = [R(1 T) − R(0 T)] (in Ω) and the normalized MR = [R(1 T) − R(0 T)]/R(0 T) (in %) of two such bridges versus temperature. The results are plotted in figures 4(b) and (d), where we chose to present data of two
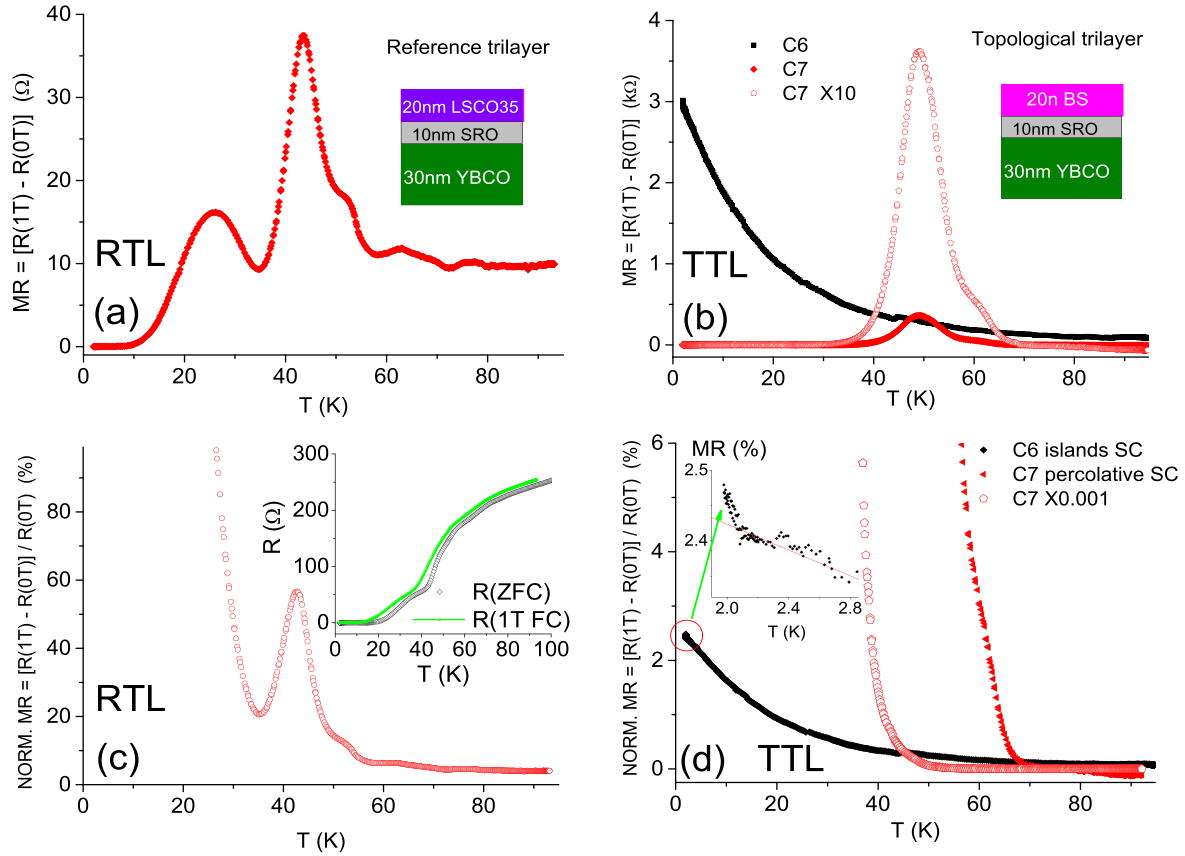
Figure 4. Magnetoresistance versus temperature of $10 \times 100 \ \mu m^2$ microbridges of a RTL of 20 nm LSCO35 on 10 nm SRO on 30 nm YBCO is given in (a) and (c), and that of the the resistive (C6) and superconductive (C7) microbridges of the TTL of figure 2(c) is shown in (b) and (d). The magnetoresistance is defined here as MR = $R(1 \, T) - R(0 \, T)$ and its normalized value as $[R(1 \, T) - R(0 \, T)]/R(0 \, T)$. For the superconductive microbridges $R(0 \, T) \rightarrow 0$ at low temperature, thus their corresponding normalized MR diverges. The inset of (c) shows the R (ZFC) and $R(1 \, T \, FC)$ versus temperature of the RTL, and that of (d) is a zoom-in on the low temperature normalized MR of the resistive bridge C6 of figure 2(c).

adjacent bridges one resistive and insulating (C6) and the other metallic and superconducting (C7). For comparison we also show in figures 4(a) and (c) MR results measured on one bridge of the RTL where a metallic LSCO35 layer replaces the topological BS layer in the trilayer. Since the MR data of the RTL is more easily interpreted and similar to the previously reported MR measurements on 5–50 nm LSCO35/ 5 nm LSCO12 [32], we shall discuss it first. In figure 4(a) of the RTL one sees two dominant peaks at 37 and 26 K, with leading edges on their high temperature side at 55 and 35 K, respectively. (The additional small peaks at higher temperatures originate in more oxygenated regions at the inner parts of the YBCO grains, and will not be discussed here.) The main peak originates in the superconducting transition of the YBCO grains, and the one on its left is a result of the second transition (see inset to figure 4(c)) due to proximity effect of these YBCO grains with the cap layer of LSCO35/SRO. Both MR peaks are formed due to two competing phenomena, flux flow against flux pinning. On cooling down below T_c at about 55 K, the MR is increasing rapidly due to increasing flux flow. By further lowering the temperature, pinning of flux also increases and as a result the MR decreases too, forming the main peak. In a stand-alone YBCO layer, this continues until there is no flux motion and the

resistance goes to zero. Here however we have a trilayer and due to the proximity effect in it, there is a second superconductive transition at lower temperature as seen in the inset to figure 4(c). Therefore, a second PE MR peak due to this transition is developed at low T, but in this case the resistance does go to zero below it. This effect is clearly seen in figure 4(c) where the normalized MR diverges at low T. The main MR peak is still clearly seen, but from the second PE MR peak only the leading edge remains.

We now turn to the MR results of the TTL. Figure 4(b) shows a single MR peak for the superconductive C7 bridge of figure 2(c), similar to the main MR peak of the RTL bridge in figure 4(a). The second PE MR peak as in the RTL is now absent or within the noise of the measurements. This indicates that the PE in the TTL is strongly suppressed as compared to that of the RTL. Since the only difference between the TTL and the RTL is the top BS layer, we conclude that the PE suppression in the TTL is due to the apparently strong surface currents in the topological layer at the interface with the SRO. We know of no theory that predicts this strong PE suppression behavior with a topological material. The MR versus T of the resistive C6 bridge looks quite different from that of the superconductive C7 bridge, but actually it is not. Its' slow and broad increasing MR below about the same 65 K, seems to be
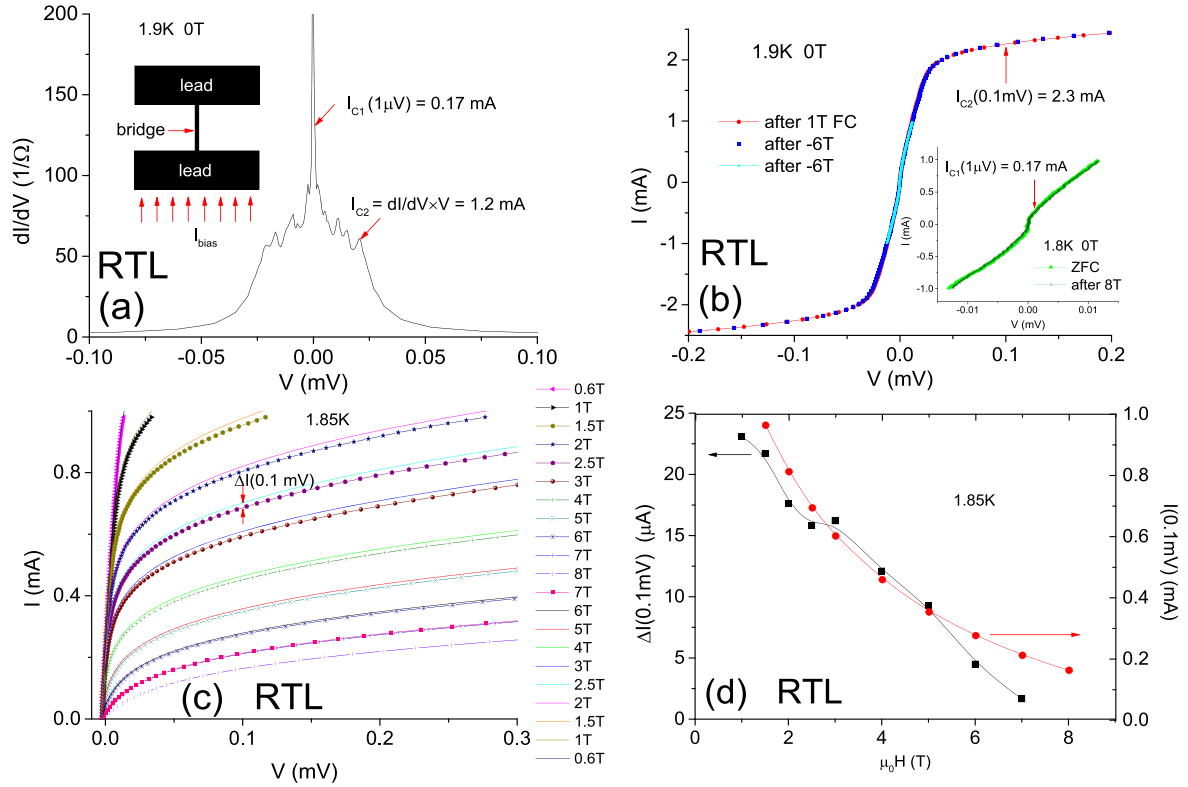
Figure 5. (a) A conductance spectrum of a 10×100 μm^2 bridge (see inset) of the RTL of figures 4(a) and (c) (20 nm LSCO35 on 10 nm SRO on 30 nm underdoped YBCO). (b) depicts IVCs of this RTL bridge at 1.9 K and 0 T after various field cycling histories. No hysteresis is observed at 0 T. (c) shows many IVCs at 1.85 K under increasing and decreasing field, with hysteresis where larger currents are found at the same V-bias under decreasing field. In (d) ΔI and I at 0.1 mV of the IVCs in (c) are given versus field. The curves are just guides to the eye.

the leading edge of a very broad MR peak, just like an extended region of the C7 peak between 65 and 55 K. This indicates that transport in the C6 bridge occurs between superconducting islands which are coupled by the TI-FM cap layer. In figure 2(c) however, only a shallow plateau is observed for C6 around 50–70 K with no signature of a superconductive transition. This is apparently due to the much higher resistance of the resistive bridges as compared to the superconductive ones above T_c. A similar islands superconductivity was observed in bilayers of non-superconducting LSCO35 and superconducting underdoped $La_{1.88}Sr_{0.12}CuO_4$ [32]. Thus to summarize, the conduction mechanisms in figure 2(c) are such that C7 has a percolative SC while C6 has islands SC. The origin of the faster MR increase near 2 K in the inset of figure 4(d), seems to be due to increasing slope of the MR peak. It cannot be due to the Kondo effect, since it increases rather than decreases with increasing field.

In the following we study in more details the RTL properties with and without magnetic fields. Figure 5(a) depicts a conductance spectrum of the RTL bridge of figures 4(a) and (c) at 0 T after ZFC, with a schematic drawing of the bridge and its leads in the inset. This spectrum shows two critical currents I_{c1} and I_{c2} which are attributed to the bridge and its leads, respectively. In figure 5(b) a few IVCs are given at zero field again, but this time after various field cycling histories. The I_{c1} and I_{c2} are marked on these curves using different voltage criterions or methods of calculation than in (a). Clearly, for bias current above I_{c1}, the

bridge becomes resistive as seen by the slope at low bias in (b), but at higher bias the second I_{c2} of the leads is observed. The 0.1 mV criterion for this supercurrent was chosen arbitrarily for convenience. No hysteresis was observed in (a) and (b) under zero field. In figure 5(c) several IVCs at 1.85 K are shown under increasing field up to 8 T followed by decreasing it back to 0 T. One can easily see that hysteresis is observed between 1 and 7 T after this field cycling. We use $\Delta I(0.1$ mV$)$ as a measure of this hysteresis, and plot it versus field in figure 5(d) together with the corresponding currents I under decreasing fields. The hysteresis clearly results from the ferromagnetic SRO layer of the RTL. Although this layer is present also in the TTL, no such hysteresis effects were observed in the TTL. This is a clear indication for strong suppression of the ferromagnetic properties by the topological layer, which is an effect similar to the previously observed suppression of the superconductive PE.

To further study the hysteresis effect of the RTL, we now look for a signature of the coercive field (H_{Coer}) of the SRO in this trilayer. Previously, we found H_{Coer} of about 1 T in similar 15 nm BST/15 nm SRO bilayers [11]. Here the SRO layer is thinner, only 10 nm thick, thus a higher H_{Coer} is expected. Figure 6(a) shows the dynamic resistance $R_d = dV/dI$ at 1.85 K derived from the IVCs of figure 5(c) at 0.1 mV. A B-spline fit to the data and a linear fit through a selected set of data points are also depicted in this figure. To identify a peak in the data of (a) at H_{Coer} we first take the field derivative of the B-spline fit. The result is plotted in (b) where
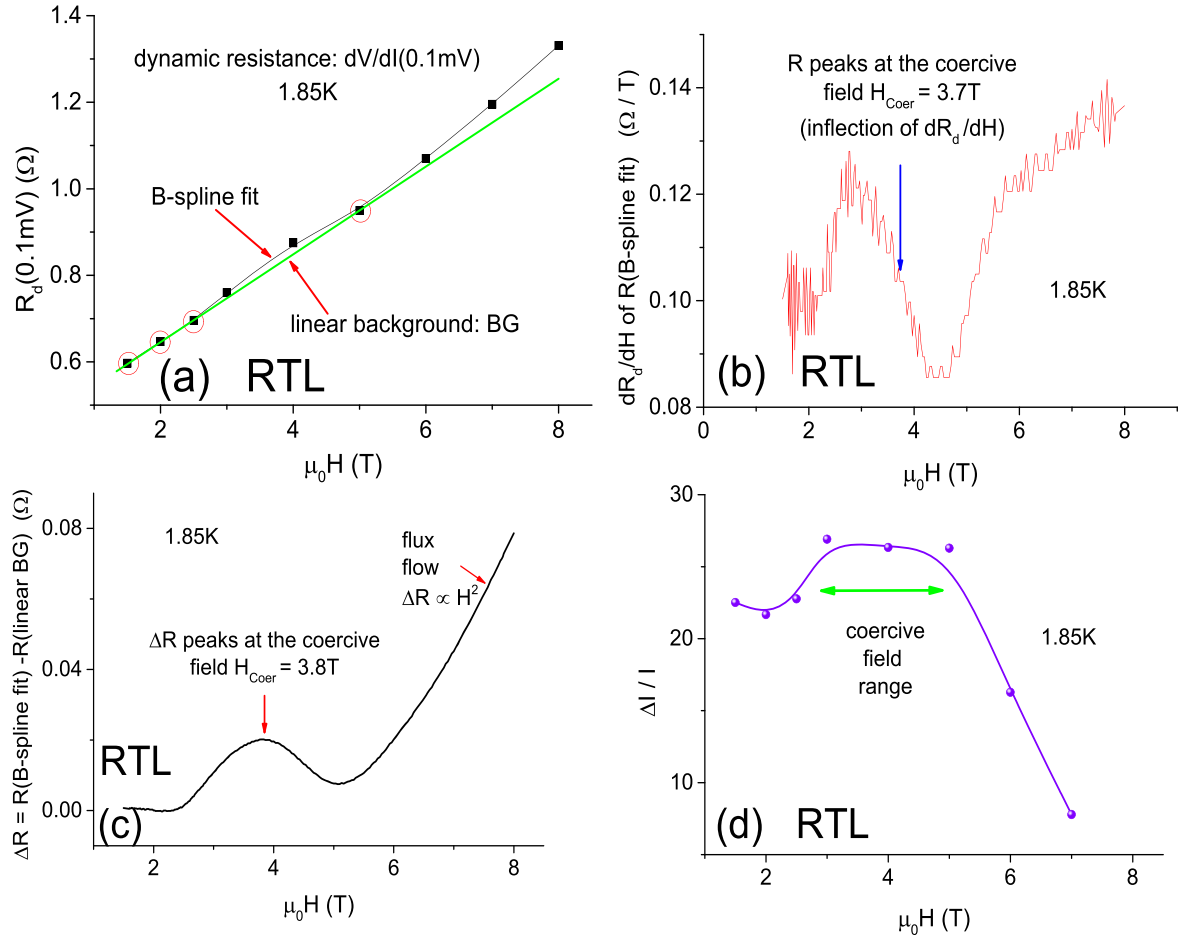
Figure 6. Dynamic resistance R_d of the RTL of figures 4(a) and (c), using the IVCs of figure 5(c), is shown at 1.85 K and 0.1 mV in (a) versus magnetic field H. A linear fit background (BG, the green line) is obtained using the four encircled data points, and the B-spline fit is calculated using all data points. (b) Shows the field derivative of the B-spline fit of (a), while (c) depicts ΔR which is the difference between R of the B-spline fit of (a) and the linear background BG at the same H. (d) Shows $\Delta I/I$ using the data of figure 5(d) versus field.

the inflection point indicates the field where R_d peaks which leads to H_{Coer} of 3.7 T. Alternatively, if we consider the linear fit in (a) as background (BG), we can subtract it from the B-spline fit and the result is depicted versus field in (c). Here we can clearly see the coercive field peak at 3.8 T which is almost equal to that obtained from (b) to within the noise of the derivative curve. The parabolic behavior of ΔR at high fields in (c) is common, and due to weak flux flow that still remains at this low temperature [33]. H_{Coer} value around 4 T can also be found from a plot of $\Delta I/I$ (calculated from the data of figure 5(d)) versus H which is given in figure 6(d). This data is quite scattered and therefore only a range of maximum $\Delta I/I$ can be obtained between 3 and 5 T, which agrees with the values found earlier. We conclude from figures 5 and 6 that the ferromagnetic properties of the SRO layer in the RTL are robust, while in the TTL they are strongly suppressed as in figure 3. We attribute this suppression, as well as that of the superconductive PE MR of figures 4(b) and (d), to lattice and Fermi levels mismatch and to unfavorable effects of strong spin–orbit coupling in BS on the d-wave pairing of YBCO with its short coherence length.

Next we look for signatures of MFs in our data. For this we chose to present data measured on a different topological

trilayer TTL-2, whose resistive bridges have one to three orders of magnitude higher resistance than that of our previous TTL of figures 2(c). The results are shown in figure 7 where (a) depicts R versus T of six bridges on this wafer. Compared to the resistance of the C6 bridge of figure 2(c) at about 2 K, the C8 bridge here has about thousand times higher resistance while the C5 bridge is ten times more resistive. Figures 7(b)–(d) show IVCs and conductance spectra of the two bridges at about 1.9 K and under various fields. Figure 7(b) shows the data for the most resistive C8 bridge, which depicts a single prominent ZBCP at 0 T that is strongly suppressed by field. Also seen are a few much weaker bound state peaks and knees whose V-values are field dependent. The data of the two orders of magnitude less resistive C5 bridge of (c) and (d) is not as clear cut. While the tunneling nature of these spectra is clearly seen and both have ZBCPs, many additional peaks also appear asymmetrically at different V-values which depend on the applied field. We note that even under 0 T, an internal field exists in the trilayer due to the magnetization of the SRO layer. To qualitatively understand these results, we refer to the model in figure 1(d), and in particular to the area enclosed by the dashed rectangle. As already discussed earlier, our trilayers with underdoped
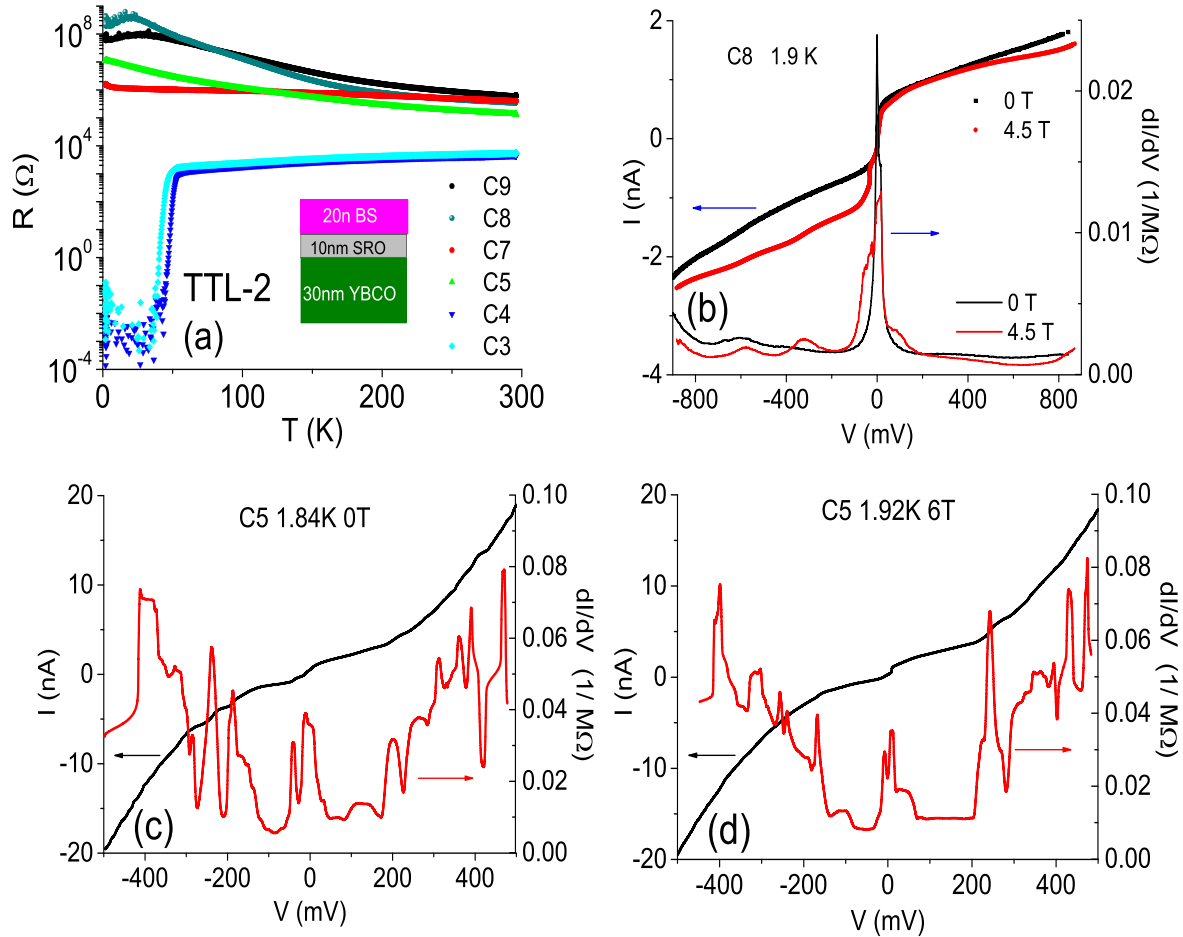
Figure 7. (a) R versus T of six microbridges on a different topological trilayer TTL-2 whose resistive bridges have one to three order of magnitude higher resistance than that of our previous TTL of figure 2(c). IVCs and conductance spectra of the C8 and C5 bridges at about 1.9 K are depicted in (b)–(d). In (b) the magnetic fields are 0 and 4.5 T, while in (c) and (d) they are 0 and 6 T, respectively.

YBCO form a network of isolated YBCO grains, thus current cannot flow directly between these grains but can flow via the BS/SRO cap layer. The edge currents in the topological BS layer are marked schematically in figure 1(d) by the two bold black arrows. If this is the actual scenario, then the edge current closer to the interface induces a proximity edge current in the adjacent SRO/YBCO layers (see the thin black arrow in figure 1(d)). In this case, one can use the model given by Beenakker [20] and conclude that a spatially split pair of MFs exists (the red dots in figure 1(d)) which is bound by the magnetic Zeeman gap and the superconducting gap on both sides, thus leading to a MBS at zero bias in the present system. This bound state in turn will increase the density of states at zero bias, which will lead to a ZBCP in the conductance spectra. ZBCPs in general can also originate in Andreev bound states (ABSs) [31, 34], but the presently observed ZBCPs in figures 7(b)–(d) are consistent with the MBS scenario just as well. In a network of isolated superconducting grains as in figure 1(d), there can be many MBSs which also interfere with one another. Thus the many other peaks beside the ZBCPs in (c) and (d) can be a result of such interference or due to non-zero bias ABSs. The derivatives dI/dV in figures 7(c) and (d) though are quite noisy, and some of the peaks could originate in noise. Therefore, it is even

better to look at the original IVCs, all of which have a step at zero bias, that leads to the ZBCPs. We attribute these steps to MBSs, but they could also result from residual small supercurrent inside the YBCO grains. Thus we conclude that the observed ZBCPs could originate in MBSs, but ABSs and small supercurrents could not be ruled out as their source. Moreover, for the bridge with the highest resistance (C8), a smaller number of weaker peaks are found in the conductance spectra besides the ZBCP, as compared to the C5 results. This is very reasonable considering that in the 1D network of channels (the weak-links) via which the current flows between the YBCO grains, a higher resistance means that less channels are open for this flow. Thus fewer channels give rise to a robust ZBCP with very little interference peaks, as we actually observed.

Finally, we discuss the potential of the present trilayers with their 1D network of weak-link channels, as a possible platform for Majorana electronics. We compare our results to the recent work by the Marcus group [22], which also reports on a 1D artificial network of SC/TI wires grown selectively on a wafer, without an FM layer but with gating. Both systems could be useful for Majorana electronics since they facilitate braiding of MBSs necessary for quantum computing. But while our 1D network is disordered and hard to

control at the present time, theirs is ordered, have good control and is much more advanced. Nevertheless, the operational temperatures of their devices are at the tens of milii Kelvins, while ours can be easily operated at a few Kelvins due to the much higher T_c of YBCO (50 K here) versus Al (1.2 K). Possibly, a combination of the two techniques, namely selective growth or patterning of the wires in an ordered network, and the use of a SC with a higher T_c instead of Al, would yield a more acceptable and controllable system for practical applications. We conclude with a few remarks on our TTLs. As seen in figure 7(b), it is desirable to use highly resistive bridges for producing MBSs. It is also expected that patterning of much smaller nano-bridges in the present TTLs would allow to isolate a smaller number of MBSs, thus reducing the number of interference peaks. Moreover, the use of other topological materials such as semiconductors with strong spin–orbit interaction and good lattice match with the base SRO/YBCO bilayer, instead of the presently used BS, is expected to lead to all-epitaxial trilayers with much better control of the MBSs properties. This could open the way for the use of such TTLs as a possible platform for Majorana based nano-electronics on standard wafers.

4. Conclusions

To summarize, microbridges patterned in the TTL of the underdoped 60 K YBCO phase showed either percolative superconducting behavior or resistive tunneling conductance between YBCO islands via the BS/SRO cap layer. Signatures of the comprising BS and SRO layers of the TTL were found, where WAL in the magnetoresistance of the BS layer and asymmetry in the tunneling conductance spectrum of the SRO layer were observed. Compared to the RTL results, we found a strong suppression of the superconductive PE as well as the ferromagnetic properties in the TTL. This is attributed to lattice and Fermi level mismatch and to unfavorable effects of strong spin–orbit coupling in BS on the d-wave pairing of YBCO. Observed ZBCPs in our conductance spectra in highly resistive TTL brides is consistent with the presence of MBSs.

ORCID iDs

Gad Koren ⬤ https://orcid.org/0000-0001-8741-1010

References

[1] Koren G, Kirzhner T, Kalcheim Y and Millo O 2013 Signature of proximity-induced $p_x + ip_y$ triplet pairing in the doped topological insulator Bi_2Se_3 by the s-wave superconductor NbN *Europhys. Lett.* **103** 67010

[2] Fu L and Berg E 2010 Odd-parity topological superconductors: theory and application to $Cu_xBi_2Se_3$ *Phys. Rev. Lett.* **105** 097001

[3] Alidoust M, Halterman K and Valls O T 2015 Zero-energy peak and triplet correlations in nanoscale superconductor/ferromagnet/ferromagnet spin valves *Phys. Rev.* B **92** 014508

[4] Kalcheim Y, Millo O, Di Bernardo A, Pal A and Robinson J W A 2015 Inverse proximity effect at superconductor-ferromagnet interfaces: evidence for induced triplet pairing in the superconductor *Phys. Rev.* B **92** 060501(R)

[5] Hassan M Z and Kane C L 2010 Colloquium: topological insulators *Rev. Mod. Phys.* **82** 3045–67

[6] Kitaev A Y 2003 Fault-tolerant quantum computation by anyons *Ann. Phys.* **303** 2–30

[7] Koren G and Kirzhner T 2012 Zero-energy bound states in tunneling conductance spectra at the interface of an s-wave superconductor and a topological insulator in NbN/Bi_2Se_3/Au thin-film junctions *Phys. Rev.* B **86** 144508

[8] Koren G 2015 Proximity effects at the interface of a superconductor and a topological insulator in NbN–Bi_2Se_3 thin film bilayers *Supercond. Sci. Technol.* **28** 025003

[9] Fan Y, Ghatak S, Taskin A A, Segawa K, Ando Y, Shiraishi M, Kanai Y, Matsumoto K, Rosch A and Ando Y 2016 Switching of charge-current-induced spin polarization in the topological insulator $BiSbTeSe_2$ *Phys. Rev.* B **94** 075304

[10] Wei P, Katmis F, Assaf B A, Steinberg H, Jarillo-Herrero P, Heiman D and Moodera J S 2013 Exchange-coupling-induced symmetry breaking in topological insulators *Phys. Rev. Lett.* **110** 186807

[11] Koren G 2018 Magnetic proximity effect of a topological insulator and a ferromagnet in thin-film bilayers of $Bi_{0.5}Sb_{1.5}Te_3$ and $SrRuO_3$ *Phys. Rev.* B **97** 054405

[12] Mourik V, Zuo K, Frolov S M, Plissard S R, Bakkers E P and Kouwenhoven L P 2012 Signatures of Majorana fermions in hybrid superconductor-semiconductor nanowire devices *Science* **336** 1003–7

[13] Das A, Ronen Y, Most Y, Oreg Y, Heiblum M and Shtrikman H 2012 Zero-bias peaks and splitting in an Al–InAs nanowire topological superconductor as a signature of Majorana fermions *Nat. Phys.* **8** 887–95

[14] Albrecht S M, Higginbotham A P, Madsen M, Kuemmeth F, Jespersen T S, Nygård J, Krogstrup P and Marcus C M 2016 Exponential protection of zero modes in Majorana islands *Nature* **531** 206–9

[15] Alidoust M, Zyuzin A and Halterman K 2017 Pure odd-frequency superconductivity at the cores of proximity vortices *Phys. Rev.* B **95** 045115

[16] Alidoust M and Halterman K 2018 Half-metallic superconducting triplet spin multivalves *Phys. Rev.* B **97** 064517

[17] Kuerten L, Richter C, Mohanta N, Kopp T, Kampf A, Mannhart J and Boschker H 2017 In-gap states in superconducting $LaAlO_3$–$SrTiO_3$ interfaces observed by tunneling spectroscopy *Phys. Rev.* B **96** 014513

[18] Hao Z *et al* 2018 Quantized Majorana conductance *Nature* **556** 74

[19] Chun-Xiao L, Sau J D, Stanescu T D and Das Sarma S 2017 Andreev bound states versus Majorana bound states in quantum dot-nanowire-superconductor hybrid structures: trivial versus topological zero-bias conductance peaks *Phys. Rev.* B **96** 075161

[20] Beenakker C W J 2013 Search for Majorana fermions in superconductors *Annu. Rev. Condens. Matter Phys.* **4** 113–36

[21] Aguado R 2017 Majorana quasiparticles in condensed matter *La Riv. Nuovo Cimento* **11** 523–93

[22] Vaitiekenas S, Whiticar A M, Deng T M, Krizek F, Sestoft J E, Marti-Sanchez S, Arbiol J, Krogstrup P, Casparis K and Marcus C M 2018 Selective area grown semiconductor-

superconductor hybrids: a basis for topological networks arXiv:1802.04210 [cond-mat.mes-hall]

[23] Koren G, Gupta A, Giess E A, Segmuller A and Leibowitz R B 1989 Epitaxial films of YBa$_2$Cu$_3$O$_{7-\delta}$ on NdGaO$_3$, LaGaO$_3$ and SrTiO$_3$ substrates deposited by laser ablation *Appl. Phys. Lett.* **54** 1054–6

[24] Marshall A F, Klein L, Dodge J S, Ahn C H, Reiner J W, Mieville L, Antagonazza L, Kapitulnik A, Geballe T H and Beasley M R 1999 Lorentz transmission electron microscope study of ferromagnetic domain walls in SrRuO$_3$: statics, dynamics, and crystal structure correlation *J. Appl. Phys.* **85** 4131–40

[25] Klein L, Kats Y, Marshall A F, Reiner J M, Geballe T H, Beasley M R and Kapitulnik A 2000 Domain wall resistivity in SrRuO$_3$ *Phys. Rev. Lett.* **84** 6090

[26] Butch N P, Kirshenbaum K, Syers P, Sushkov A B, Jenkins G S, Drew H D and Paglione J 2010 Strong surface scattering in ultrahigh-mobility Bi$_2$Se$_3$ topological insulator crystals *Phys. Rev. B* **81** 241301(R)

[27] Zhang H, Liu C-X, Qi X-L, Xi D, Fang Z and Zhang S-C 2009 Topological insulators in Bi$_2$Se$_3$, Bi$_2$Te$_3$ and Sb$_2$Te$_3$ with a single Dirac cone on the surface *Nat. Phys.* **5** 438–42

[28] Koren G 2017 Magnetoresistance, gating and proximity effects in ultrathin NbN–Bi$_2$Se$_3$ bilayers *Condens. Matter* **2** 14

[29] Hikami S, Larkin A I and Nagaoka Y 1980 Spin-orbit interaction and magnetoresistance in the two dimensional random system *Prog. Theor. Phys.* **63** 707–10

[30] Tedrow P M and Meservey R 1973 Spin polarization of electron tunneling from films of Fe, Co, Ni and Gd *Phys. Rev. B* **7** 318–26

[31] Aronov P and Koren G 2005 Signature of a crossed Andreev reflection effect in the magnetic response of YBa_2Cu$_3$O$_{7-\delta}$ junctions with the itinerant ferromagnet SrRuO$_3$ *Phys. Rev. B* **72** 184515

[32] Koren G and Millo O 2009 Conventional proximity effect in bilayers of superconducting underdoped La$_{1.88}$Sr$_{0.12}$CuO$_4$ islands coated with nonsuperconducting overdoped La$_{1.65}$Sr$_{0.35}$CuO$_4$ *Phys. Rev. B* **80** 054507

[33] Tinkham M 1988 Resistive transition of high-temperature superconductors *Phys. Rev. Lett.* **61** 1658–61

[34] Tanaka Y and Kashiwaya S 1995 Theory of tunneling spectroscopy of d-wave superconductors *Phys. Rev. Lett.* **74** 3451–4